Lifetime Estimation of Grid-Connected Battery Storage and Power Electronics Inverter Providing Primary Frequency Regulation

MARCO STECCA[1], (Student Member, IEEE), THIAGO BATISTA SOEIRO[1], (Senior Member, IEEE), LAURA RAMIREZ ELIZONDO[1], (Member, IEEE), PAVOL BAUER[1], (Senior Member, IEEE), and PETER PALENSKY[1], (Senior Member, IEEE).

[1]Electrical Sustainable Energy Department, Delft University of Technology, Delft, 2628 CD, NL.

Corresponding author: Marco Stecca (e-mail: m.stecca@tudelft.nl).

ABSTRACT Battery Energy Storage Systems (BESSs) are a new asset for Primary Frequency Regulation (PFR). PFR consists of varying the generator's power output proportionally to the grid frequency deviations, so to preserve the grid stability. The implementation and remuneration of PFR are determined by the system operators. However, assessing the revenue stream is not enough to define the business case, as also the components' lifetime has to be estimated. Previous studies of lifetime estimation for BESSs performing PFR considered only the electrochemical storage, disregarding the power electronics (PE). Nonetheless, researchers have shown the importance of estimating PE wear due to the operation when applied in renewable energy generation and microgrids. This paper presents a lifetime analysis of BESSs providing PFR considering IGBT modules, electrolytic capacitors and electrochemical storage degradations. The lifetime information is used to estimate BESS's Net-Present-Value (NPV), therefore evaluating the benefits of deploying PE-based BESS in the European grid. A comparison between different countries, Germany, Netherlands, and UK, is performed, considering the PFR implementation and remuneration differences. The analysis shows that the BESS management strategy can extend its lifetime and that the component that exhibits the shortest lifetime is the electrochemical storage. In conclusion, the provision of PFR by means of BESS has been found to be profitable, especially in the Netherlands.

INDEX TERMS Battery Energy Storage System, Primary Frequency Regulation, Voltage Source Converter, lifetime estimation, Net Present Value.

I. INTRODUCTION

THE rising of renewable energy based generation plants is shifting the electrical energy production from large synchronous generators to Power Electronics (PE) interfaced distributed plants. Consequently, the inertia of the system and its regulating power, traditionally provided by large rotating synchronous generators, will likely decrease [1], [2]. System operators are then in the need of finding new balancing resources. In this context, new assets are entering the grid balancing ancillary services, i.e., wind turbines [3], photovoltaic generators [4], and energy storage systems [5].

Battery Energy Storage Systems (BESSs), a technology characterized by high efficiency and relatively fast response [6], are particularly suitable for various balancing services, as grid inertial response [7], frequency nadir and Rate of Change of Frequency (RoCoF) reduction [8], and Primary Frequency Regulation (PFR) [9]–[11]. PFR consists of varying the generator's power output proportionally to the fundamental frequency deviations from the nominal value, i.e., 50 Hz in Europe and China, and 60 Hz in America. The technical implementation and remuneration of PFR in Europe are regulated by the national Transmission System Operators (TSOs) and it may differ between countries [12], [13]. BESSs are an emerging asset for PFR, also due to the clearly regulated remuneration, as opposed to other potential BESSs applications, i.e. voltage control, congestion management, peak shaving.

Although Lithium-ion BESSs show good technical suitability for PFR [14], [15], the high initial investment required to deploy such systems represents a barrier for system oper-

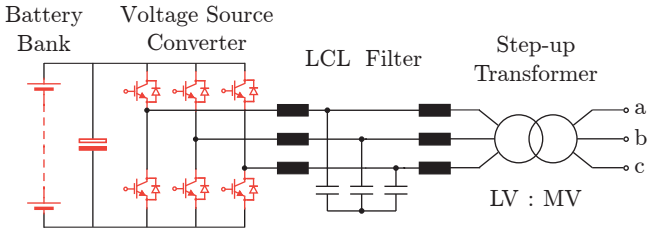

FIGURE 1. Circuit schematic of a grid-connected BESS with the critical components in terms of lifetime highlighted in red.

ators and private investors [16], [17]. Consequently, BESS's lifetime becomes a key factor for defining its business case.

Most high power commercial BESSs, e.g. from 100 kW to 5 MW, are based on a two level Voltage Source Converter (VSC), constructed with three half-bridge legs for interfacing the battery bank with a Low Voltage (LV) AC grid [18], [19]. Additionally, a LCL filter is used to contain the current harmonics injection inside the limits regulated by standards [20], and when needed an auxiliary transformer is used to step up the voltage for the connection to the Medium Voltage (MV) grid. The described high power BESS system is shown in Fig. 1. Other elements, not shown in Fig. 1, exists for protection, such as AC and DC contractors, and electromagnetic compatibility filters.

Research in power electronic reliability shows that the main components within the VSCs subject to failure due to wear are the IGBT modules and the DC-link electrolytic capacitors [21]–[24]. Additionally, Lithium-ion based batteries have a limited lifetime, strongly influenced by the cycling pattern [25], and which generally spans from 3000 to 10000 cycles, depending on the lithium technology and on the cycling conditions [26]. The IGBT modules, the electrolytic capacitors, and the electrochemical storage are then the components that are the most subject to wear in a BESS.

The degradation of IGBTs and electrolytic capacitors is mainly driven by the thermal stress to which they are subjected [27], [28], the electrochemical storage's degradation, instead, is mostly driven by its cycling pattern [25], [26]. In this respect, the lifetime of the battery cells providing PFR has been already investigated [15], nonetheless, in these studies the power electronic components have not been considered. Instead, prior research on PE converter lifetime has focused on other applications, such as wind and solar generation [27], [29]–[31], microgrids [28], and aerospace [32]. However, power electronic plays a major role in BESSs, being the enabler technology used to interface the electrochemical storage with the AC grid. Above all, the PE wear constitute an important factor to be evaluated when studying BESS's lifetime [24].

This paper presents a mission profile based lifetime analysis of BESSs performing PFR as ancillary grid service. The choice of this grid service is driven by the well defined technical, economical and regulatory framework of PFR,

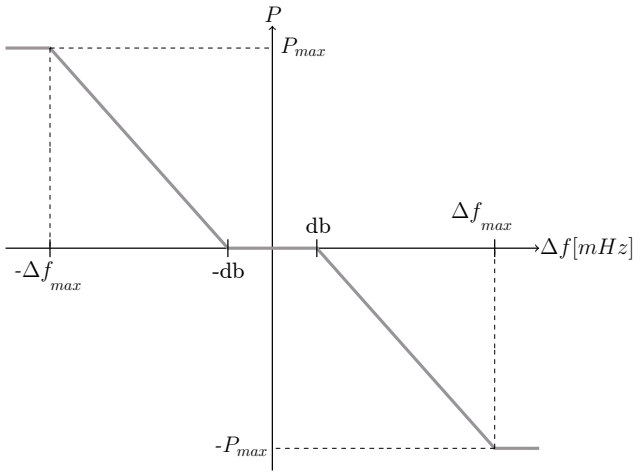

FIGURE 2. Example of a P-f droop control curve for PFR provision.

which allows the definition of a positive BESS's business case. The lifetime is defined by investigating the degradation of IGBT modules, electrolytic capacitors, and electrochemical storage. The components' lifetime models adopted, derived through accelerated lifetime testing, are taken from the manufacturers [33]–[35] and from the literature [36], [37]. Additionally, three case studies, particular to Germany, the United Kingdom (UK), and the Netherlands, with their differences in terms of technical implementation and remuneration, are considered. To conclude, the economic viability of BESSs deployed to perform PFR is evaluated, based on the information about components' replacement derived from the lifetime analysis.

The contribution of this paper is twofold: first, a mission profile based methodology to evaluate the lifetime of BESSs that considers electrochemical storage and power electronics wear is proposed. The methodology is general, it can be used to estimate BESS's component lifetime for any BESS application. Second, technical and economical insights are presented after applying this methodology on a case study in which BESSs provide PFR in three European countries. More specifically, the lifetime information, derived from analysing electrochemical storage and PE wear, is used to estimate BESS's Net-Present-Value (NPV). This allows to evaluate the economic benefits of deploying PE-based BESS for the provision of ancillary services to the grid. The benefits are determined by comparing three case scenarios, reflecting three different energy markets in Europe, namely, Germany, the Netherlands, and the UK. The study considers the standardized PFR implementation, the BESS State-of-Charge (SoC) management, and the remuneration schemes. In this way, this paper also aims at highlighting how BESSs' lifetime and business case are influenced by the existing differences between the countries where the technology is applied.

II. PRIMARY FREQUENCY REGULATION MARKET

Primary frequency regulation is an ancillary service typically offered by generators connected to the transmission networks

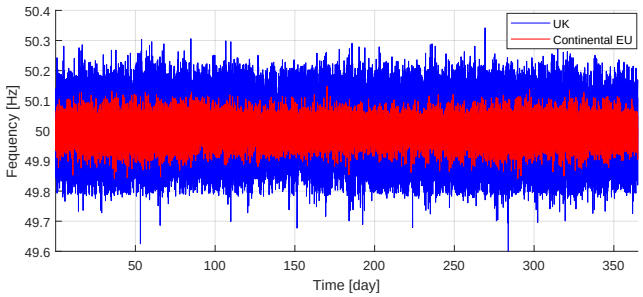

FIGURE 3. Measured frequency trend in UK and continental Europe during 2018 [38], [41].

in the ancillary service market. This service may assume different names depending on the country, however in the remainder of the paper it will be referred as PFR. PFR is a process to maintain stability in the power system by reacting to frequency variations. When a frequency change Δf occurs after a fluctuation in the generation or load, the PFR operates to adjust the active power output of the generators and other available controllable units in the system, such as BESSs. The power output is adjusted according to a droop characteristic that follows Δf. An example of such droop control logic is shown in Fig. 2. Both UK and Germany adopt a deadband, which is a frequency interval around the nominal value in which the system is not required to exchange power with the grid. This deadband has a different amplitude for UK and Germany, i.e. $\pm$15mHz and $\pm$10mHz respectively [12], [38], [39]. In the Netherlands, an insensitivity range of $\pm$10mHz is implemented instead [40]. The insensitivity range acts as a moving deadband, requiring the unit to change its power output only if a frequency variation greater than 10 mHz from the current operating point is detected [40]. Despite the differences in the deadband and insensitivity range, in all three countries the maximum regulating power has to be delivered for frequency variations higher than a preset threshold, i.e., 200 mHz in Germany and the Netherlands, and 500 mHz in the UK [38]–[40]. Additionally, energy limited resources, such as BESSs, are required to be able to keep the maximum power for frequency variations $\geq$200 mHz for at least 15 or 30 minutes. The minimum required power of generators and BESSs providing such service is generally $>$1MW. However, owners of multiple sources of low power grid assets, such as stationary batteries, industrial processes, renewable energy generation, and Electric Vehicles (EVs) charging stations, can cluster their power capability together to deliver the minimum required power [10], [38]–[40].

To participate in the PFR market, Balance Service Providers (BSPs) submit their bids to the responsible TSO. The bids are composed of the available regulating power and the required price for activation. Each TSO defines how much regulating power must be available in their control area at each instant; with this information they set up the tenders. After collecting all BSPs's bids, the cheapest feasible bids (that guarantee the required regulating power in the area) are

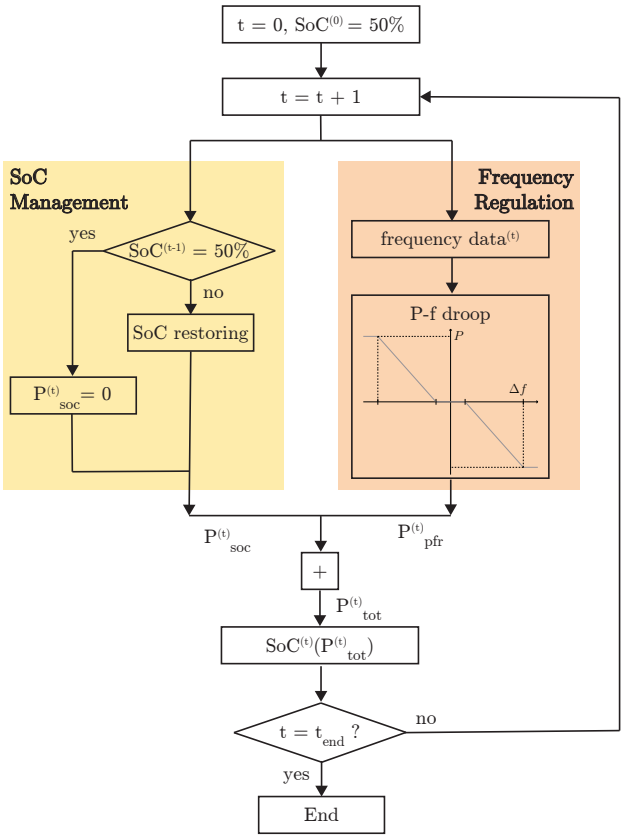

FIGURE 4. Flowchart describing the algorithm for PFR provision, where t indicates the time instant and P^t_{pfr} and P^t_{SoC} are respectively the frequency regulation power and the SoC control power at the instant t.

selected.

The frequency trend of continental Europe and the UK during the year 2018 are plotted in Fig. 3 [39], [42]. From this figure, it is possible to see that in the UK, the grid frequency is subject to wider variations than in continental Europe; this is due to the lower inertia of the system. By following the frequency oscillations, energy limited resources, such as BESSs, will inevitably see a deviation of their SoC. Then, to ensure the continuous availability of the system in providing frequency regulation, the SoC of the battery has to be controlled. In this context, a fraction of the BESS power can be reserved for managing the SoC and for keeping it close to a reference value. Consequently, the frequency regulation service is provided only with the remaining available power. Alternatively, when the deadband is contemplated in the droop function, the SoC control can be done when the frequency variations are inside the deadband, and so the output power of the system for PFR should be zero. Nonetheless, a recent guidance published by National Grid, the system operator of the UK, recommends that BESSs should withhold a fraction of the power for the SoC management, and not use the deadband for regulating the SoC [43]. For these reasons, in the remainder of the paper only the SoC management through a fraction of the full system power will be considered, assuming that the sum of the maximum power for SoC management $P_{\text{SoC,max}}$

TABLE 1. BESS design specifications and components selection.

Design Parameter		Value	Components selected	
Rated VSC power	S_{n}	150kVA	IGBT modules	Infineon FF300R12KE4
DC link voltage	$V_{\mathrm{dc,n}}$	750 - 1000V	Electrolytic Capacitors	Cornell Dubilier Type 500C
AC line-to-line voltage	$V_{\mathrm{ac,ll}}$	400 V	Battery technology	$LiFePO_4$
Switching frequency	f_{s}	12 kHz	Heat Sink	From Infineon inverter stack 6PS0300R12KE3

and for the frequency regulation $P_{\mathrm{pfr,max}}$ is always equal to the maximum system power, P_{tot}:

$$P_{\mathrm{tot}} = P_{\mathrm{SoC,max}} + P_{\mathrm{pfr,max}}. \tag{1}$$

As previously mentioned, the payment for PFR is proportional to the power tendered. Then, withholding a fraction of the total power for managing the SoC would inherently reduce the revenues from the frequency regulation market. However, the power utilization of the system would reduce, and so it would advantageously extend the lifetime of the BESS. The algorithm for the provision of PFR is illustrated in Fig. 4. The SoC regulation occurs in parallel to the PFR provision, targeting the re-establishing of the SoC at 50%, so that the BESS is able to deliver symmetrically for long time both up and down regulation, with the maximum energy available, in case of a strong frequency perturbation [14], [15]. Other parallel SoC re-establishing strategies could be implemented, for example containing the SoC into a range of values, however these are not considered in this study.

III. BATTERY ENERGY STORAGE SYSTEM DESIGN

In this study, a BESS rated 150kW/150kWh has been considered, assuming that the BESS is aggregated with other BSPs to reach the minimum required power for PFR, i.e., clustering together up to 1 MW for PFR.

The VSC circuit topology consists of three half-bridge IGBT-Diode modules. A Low Voltage (LV) DC-link is taken into account, V_{dc} =750-1000V, coherently with the specifications of commercial battery racks [44], [45], and so for the connection at the Medium Voltage (MV) network, a LV/MV transformer is necessary to step up the voltage from the 400V line-to-line output of the VSC. The circuit schematic of the BESS is shown in Fig. 1 and the three components of which the lifetime is investigated, the electrochemical storage, the IGBT modules, and the electrolytic capacitors installed in the DC-link, are highlighted in red. The design specifications and the components selected, according to the procedure described in the following, are summarized in Table 1, where S_{n} stands for the rated VSC power, V_{dc} and $V_{\mathrm{ac,ll}}$ for DC link and AC line-to-line voltages and f_{s} for the VSC's operating switching frequency.

The commercially available Trench/Fieldstop IGBT4-Diode modules FF300R12KE4, capable of withstanding up to 300A at junction and case temperatures of respectively 175°C and 100°C and of the 1200V voltage class, are selected [46]. These IGBT modules are selected based on the DC voltage, the peak collector current they have to carry and to ensure that the three VSC's legs deliver an efficiency greater or equal to 97.5% at the rated power of 150 kVA. The IGBT modules of a VSC are subject to power losses due to the current conduction and hard switching. The losses in the semiconductors causes thermal stress in the semiconductor chips and module package constituents, which drives their degradation [34]. The conduction losses P_{c} and the switching losses P_{s} for a Sinusoidal Pulse Width Modulation (SPWM) controlled VSC can be analytically calculated as function of the modulation index M, the switching frequency f_{s}, equal to 12kHz in this study, the peak AC current $\hat{I}_{\mathrm{ac}}$, and the phase shift angle between the output AC voltage and current φ, through (2)-(3) for the IGBTs and (4)-(5) for the diodes [34].

$$\begin{aligned} P_{\mathrm{c,T}} = &\left(\frac{1}{2\pi} + \frac{M\cos\varphi}{8}\right)\left[v_{\mathrm{ce},25} + \mathrm{tc}_{\mathrm{vt}}\left(T_{\mathrm{j}} - 25\right)\right]\hat{I}_{\mathrm{ac}} \\ &+ \left(\frac{1}{8} + \frac{M\cos\varphi}{3\pi}\right)\left[r_{\mathrm{ce},25} + \mathrm{tc}_{\mathrm{rt}}\left(T_{\mathrm{j}} - 25\right)\right]\hat{I}_{\mathrm{ac}}^2 \end{aligned} \tag{2}$$

$$P_{\mathrm{s,T}} = \frac{f_{\mathrm{s}} E_{\mathrm{on+off}}\hat{I}_{\mathrm{ac}}}{\pi 300}\left[1 + a_{\mathrm{t}}\left(T_{\mathrm{j}} - 25\right)\right]\left(\frac{V_{\mathrm{dc}}}{600}\right)^{k_{\mathrm{vt}}} \tag{3}$$

$$\begin{aligned} P_{\mathrm{c,D}} = &\left(\frac{1}{2\pi} - \frac{M\cos\varphi}{8}\right)\left[v_{\mathrm{f},25} + \mathrm{tc}_{\mathrm{vd}}\left(T_{\mathrm{j}} - 25\right)\right]\hat{I}_{\mathrm{ac}} \\ &+ \left(\frac{1}{8} - \frac{M\cos\varphi}{3\pi}\right)\left[r_{\mathrm{f},25} + \mathrm{tc}_{\mathrm{rd}}\left(T_{\mathrm{j}} - 25\right)\right]\hat{I}_{\mathrm{ac}}^2 \end{aligned} \tag{4}$$

$$P_{\mathrm{s,D}} = \frac{f_{\mathrm{s}} E_{\mathrm{rr}}\sqrt{2}}{\pi}\left[1 + a_{\mathrm{d}}\left(T_{\mathrm{j}} - 25\right)\right]\left(\frac{\hat{I}_{\mathrm{ac}}}{300}\right)^{k_{\mathrm{i}}}\left(\frac{V_{\mathrm{dc}}}{600}\right)^{k_{\mathrm{vd}}} \tag{5}$$

where $V_{\mathrm{ce},25}$, $r_{\mathrm{ce},25}$, $v_{\mathrm{f},25}$, $r_{\mathrm{f},25}$ are the coefficients modeling the on-state losses of IGBTs and diodes at 25°C. The on-state parameters are temperature dependent, as expressed in (2) and (4), following the coefficients $\mathrm{tc}_{\mathrm{vt}}$, $\mathrm{tc}_{\mathrm{rt}}$, $\mathrm{tc}_{\mathrm{vd}}$, and $\mathrm{tc}_{\mathrm{rd}}$ whose value is summarized in Table 2. $E_{\mathrm{on+off}}$ and E_{rr} are the hard switching added turn-on and turn-off energy losses, and reverse recovery energy losses, respectively, derived for a switched voltage V_{dc} and current of 600V and 300A, junction temperature of 25°C and external gate resistance of 2Ω. k_{vt}, k_{i}, k_{vd}, a_{t}, and a_{d} are scaling coefficients for the switching

FIGURE 5. Test board for the characterization of semiconductors modules and/or TO-packaged discrete devices.

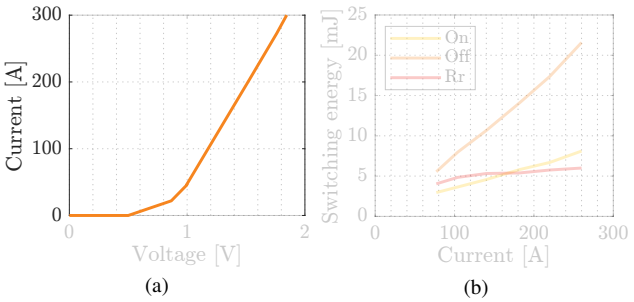

FIGURE 6. Conduction (a) and switching at $V_{\rm dc} = 600V$ (b) characteristic of the IGBT-Diode modules FF300R12KE4 measured through the test board of Fig. 5 with junction temperature of 25°C and external gate resistance of 2Ω.

energy taken from [34]. The test board shown in Fig. 5 is used to derive the on-state and switching characteristics, plotted in Fig. 6. Table 2 summarizes the coefficients and parameters used in (2)-(5) for the semiconductors losses calculations.

In order to speed up the computational time, loss-maps relating the power losses in the IGBTs and Diode to the junction temperature and converter output power are generated through (2)-(5). These are then used for the junction temperature estimation for a given mission profile. An example of the IGBT loss-map is shown in Fig. 7, where the losses in an IGBT are shown as function of its junction temperature and of the VSC output power.

Another component of the VSC of interest from the lifetime point of view is the electrolytic capacitor bank placed between the electrochemical storage and the IGBT modules, in the DC-link. The DC-link capacitors functions both as an energy buffer and they limit the DC voltage ripple. In fact, to ensure a safe and efficient DC-AC power conversion, without over modulating the PWM controlled VSC, it is required that half the DC voltage is always higher than the peak AC voltage

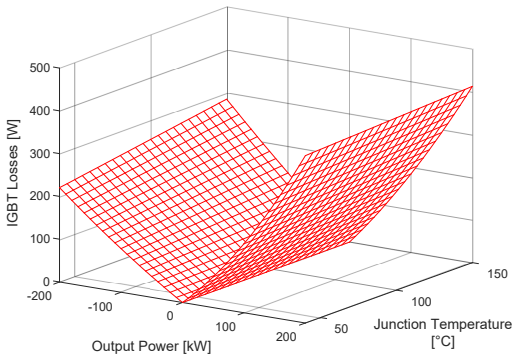

FIGURE 7. Loss-map of a single IGBT of the Trench/Fieldstop IGBT4-Diode modules FF300R12KE4 as function of its junction temperature and of the SPWM modulated at 12kHz VSC's output power, for a DC link voltage of 900V and an AC line-to-line voltage of 400V.

TABLE 2. Parameters for estimating power losses of the IGBT module FF300R12KE4 [34], [46].

IGBT		Diode	
Parameter	Value	Parameter	Value
$v_{\rm ce,25}$	0.9 V	$v_{\rm f,25}$	1.05 V
$r_{\rm ce,25}$	2.7 mΩ	$r_{\rm f,25}$	1.9 mΩ
$\rm tc_{vt}$	-0.0011	$\rm tc_{vd}$	-0.0022
$\rm tc_{rt}$	$1.28{\cdot}10^{-5}$	$\rm tc_{rd}$	$7.2{\cdot}10^{-6}$
$E_{\rm on+off}$	39 mJ	$E_{\rm rr}$	6 mJ
$a_{\rm t}$	0.003	$a_{\rm d}$	0.006
$k_{\rm vt}$	1.35	$k_{\rm vd}$	0.6
		$k_{\rm i}$	0.6

$\hat{V}_{\rm ac,max}$ [47]:

$$\frac{V_{\rm dc,min}}{2} - \frac{\Delta V_{\rm dc,r}}{2} \geq \hat{V}_{\rm ac,max}, \tag{6}$$

where $V_{\rm dc,min}$ is the minimum battery DC voltage and $\Delta V_{\rm dc,r}$ is the DC voltage ripple. In this respect, the battery's open circuit voltage variations due to the SoC, and the international grid codes, that require the normal operation for ±10% voltage deviation from the nominal value, play a crucial role. As discussed in [48], the DC-link voltage ripple $\Delta V_{\rm dc,r}$, for SPWM modulation strategy, symmetrical grid, and balanced load, is composed of only the high frequency components and it can be expressed as:

$$\Delta V_{\rm dc,r} = \frac{3M\hat{I}_{\rm ac}\cos\varphi}{8f_{\rm s}C_{\rm dc,r}}(1+M), \tag{7}$$

where $C_{\rm dc,r}$ is the DC-link capacitance value. However, in the case of unbalanced fundamental frequency loading, a second harmonic component in the DC voltage ripple arises [48]. In this case, the low-frequency component dominates the high-frequency one, and so the DC ripple takes the following expression [48]:

$$\Delta V_{\rm dc,r} = \frac{3M\hat{I}_{-}}{8\pi f_{\rm g}C_{\rm dc,r}}, \tag{8}$$

where $\hat{I}_-$ is the peak value of the negative sequence current and f_g is the grid nominal frequency of 50Hz. Equation (8) considers a three wire system, so that no zero sequence component is present. However, in this study, the balanced operation of the converter is considered and so the minimum capacitance value $C_{dc,r}$ that satisfy the DC-link voltage ripple constraint can be found combining (6) and (7).

Concerning the energy buffer functionality of the DC-link capacitors, these are sized to be able to sustain a load step of ΔP, in a time period of T_r, allowing a voltage deviation of ΔV_{dc} [49]:

$$C_{dc,e} \geq \frac{T_r \cdot \Delta P}{(2 \cdot V_{dc} \Delta V_{dc})}. \quad (9)$$

T_r depends on the DC-AC converter control delay and it is usually selected as 5 to 10 modulation periods.

The DC-link capacitance C_{dc} can be selected as the largest value between $C_{dc,r}$ and $C_{dc,e}$ that are the minimum capacitance values that ensure the fulfillment of the voltage ripple and energy buffer design requirements, derived through (6)-(9):

$$C_{dc} \geq \max\{C_{dc,e}, C_{dc,r}\}. \quad (10)$$

Additionally, the DC-link capacitors have to withstand the current flowing through them, that can be analytically calculated for the symmetric system as [50]:

$$I_{dcl} = \hat{I}_{ac} \sqrt{M \left[\frac{\sqrt{3}}{4\pi} + \left(\frac{\sqrt{3}}{\pi} - \frac{9}{16} M \right) \cos^2 \varphi \right]}. \quad (11)$$

In this study several commercially available capacitors of the $500V_{dc}$ class from [51] have been considered. Given the maximum value of I_{dcl} and the current capability of the single capacitors, the number of parallel capacitor strings, which consists of two series capacitors, are found. In this way, according to the components' characteristics, several DC-link designs are derived. The solutions that do not satisfy the minimum capacitance constraints given in (10) or that show a maximum hot-spot temperature higher than 95°C, the limit set in the data-sheet, are discarded. The volume, costs and base lifetime, that stands for the number of guaranteed hours operating at 85°C, and maximum allowed ripple current, of the remaining designs are plotted in Fig. 8. These designs respect the quality and performance constraints, and so, for further analysis, the design that offers the least cost is selected, where the commercial cost figures are derived from [52]. This is done because market competitive industrial products are often designed targeting the minimization of costs. Moreover, since grid-connected BESS are generally deployed in containers, volume minimization is not a driver as strong as the cost minimization. Additionally, in terms of power losses any substantial gain in efficiency by reducing capacitor losses would lead to prohibitive cost figures because the losses of the electrolytic capacitors are relatively much smaller than the ones seen in the semiconductors. Therefore, the design with the lowest cost that guarantees the quality and performance required, indicated with a star in Fig. 8, is selected. This DC-link configuration consists of six parallel strings of two series connected capacitors of 3.9 mF.

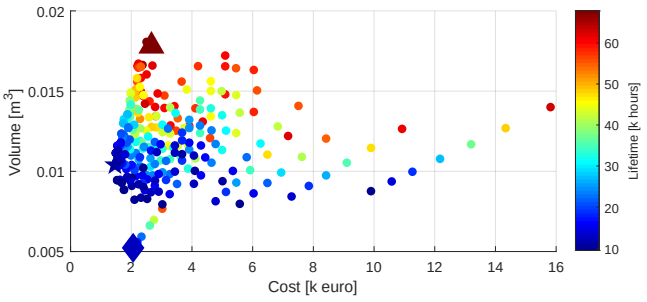

FIGURE 8. Volume, costs and lifetime of the DC-link capacitor designs that meet the design, thermal and base lifetime requirements. The star indicates the solution with the minimum cost, the diamond the one with minimum volume, and the triangle the one with maximum base lifetime.

IV. BATTERY ENERGY STORAGE SYSTEM LIFETIME MODEL

In this Section, the lifetime models for the electrochemical storage, the IGBT modules and the electrolytic capacitors are discussed.

A. ELECTROCHEMICAL STORAGE LIFETIME

Lithium-ion batteries are subject to several ageing mechanisms. This causes increase in the cell's impedance and the decrease of cyclable lithium [26], [53]. Such conditions lead to a lower battery's energy capacity, power capability, and round trip efficiency [54]. In this respect, it is common practice to consider a capacity fading of 20% as reference value for the End of Life (EoL) of grid-connected BESS and EV battery packs.

Research has shown that both the power cycling and the idling condition contribute to the ageing of Li-ion based batteries. In this study, to evaluate the electrochemical cells lifetime, the empirical model for $LiFePO_4$ batteries developed through accelerated cycling of battery cells [36] and proposed in [37] is adopted. This model has been already adopted for the estimation of battery degradation in PFR [15], [55] and wind power applications [36], [37]. The capacity fading due to calendar ageing, C_{cal}, and cycling ageing, C_{cyc}, in percentage, are then evaluated according to (12) and (13) respectively [37]:

$$C_{cal} = 0.1723 \cdot e^{0.007388 \cdot SoC_l} \cdot t^{0.8} \quad (12)$$

$$C_{cyc} = 0.021 \cdot e^{-0.01943 \cdot SoC_{avg}} \cdot cd^{0.7612} \cdot nc^{0.5}. \quad (13)$$

The capacity fading is then function of the average SoC of a cycle SoC_{avg}, the number of cycles nc of a certain cycle depth cd, and the idling time t of the battery at a certain SoC level SoC_l. Equations (12) and (13), which describe the capacity fading, are derived for a Lithium-ion battery at a

TABLE 3. Foster thermal model parameters of IGBTs, diodes and heatsink used for the study [46], [56].

	IGBT		Diode		Heatsink	
i	R [K/W]	τ [s]	R [K/W]	τ [s]	R [K/W]	τ [s]
1	0.00558	0.01	0.009	0.01	0.01374	2.23
2	0.03069	0.02	0.0495	0.02	0.04543	51.334
3	0.02976	0.05	0.048	0.05	0.0006	88.93
4	0.02697	0.1	0.0435	0.1	0.01573	88.93

temperature of 25°C. However, Lithium-ion batteries ageing is strongly influenced by the temperature [37], yet, grid connected BESS are generally deployed in containers that are equipped with air conditioning systems, used to control the temperature of the battery cells. Mostly, the temperature is kept stable at 25°C, to ensure optimal performances and extend its lifetime [55].

B. SEMICONDUCTOR LIFETIME

Power semiconductors and their packaging are subject to several failure mechanisms, such as bond wire lifting and breakage, and solder plate fatigue on the base plate and in the chip soldering [29]. These are caused by the thermo-mechanical stress induced by the temperature gradients between the components, due to the different materials and power losses [34]. In order to evaluate the junction temperature of the semiconductors, the thermal behaviour of the semiconductor and the cooling aggregate is modelled through the Foster parameters as given by the manufacturer's datasheet [46], [56]. The forced air cooling aggregate implemented in the Infineon inverter stack 6PS0300R12KE3 has been taken as reference [56]. Its Foster parameters, R_i and τ_i, used to represent the thermal behaviour of the power modules, together with the one of IGBTs and diodes, are listed in Table 3. This heatsink has been chosen to guarantee that when the VSC operates at maximum power the steady-state junction temperature does not exceed 140 °C, leaving a safe margin from 150 °C, which is the maximum allowed temperature during switching conditions according to the IGBT modules' data-sheet [46].

The number of cycle to failure N_f of an IGBT module subject to a thermal cycle of amplitude ΔT_j, minimum junction temperature $T_\mathrm{j,min}$, and with heating time t_on are estimated through:

$$N_f = A \cdot \Delta T_\mathrm{j}^{\beta_1} \cdot e^{\frac{\beta_2}{T_\mathrm{j}+273}} \cdot t_\mathrm{on}^{\beta_3} \cdot I_\mathrm{B}^{\beta_4} \cdot V_\mathrm{C}^{\beta_5} \cdot D^{\beta_6}. \quad (14)$$

Equation (14) is resulting from several empirical studies, based on power cycling of multiple IGBT modules [33], [34]. The number of cycles to failure are determined also as function of the current per bond wire I_B, the module voltage class V_C, the bond wire diameter D. The coefficient A relates to the IGBT technology and it is equal to $9.34 \cdot 10^{-4}$ for Infineon IGBT4, while $\beta_1 ... \beta_7$ are selected according to [34]. Further experimental studies have updated (14), showing how semiconductor degradation saturates with thermal cycles with load periods (t_on) longer than 60s [28], [57]. Then, the influence of the loading time, when longer than 60s, can be modelled in (14):

$$\frac{N_f\,(t_\mathrm{on})}{N_f(1.5)} = 0.33, \quad t_\mathrm{on} \geq 60\mathrm{s}. \quad (15)$$

The IGBT module's consumed lifetime due to a specific cycle p is found as the reciprocal of $N_{f,p}(\Delta T_{\mathrm{j},p}, T_{\mathrm{j},p}, t_{\mathrm{on},p})$. When the consumed lifetime reaches the unity the module is considered at the end of life. Hence, the semiconductor lifetime can be estimated as:

$$L_\mathrm{s} = \frac{1}{\sum_{p=1}^{N} CL_{\mathrm{s},p}} = \frac{1}{\sum_{p=1}^{N} \frac{n_p}{N_{f,p}}}, \quad (16)$$

where the index $p = 1...N$ represents the distinct thermal cycles and n_p the occurrences of the cycle p during a certain period of time.

C. ELECTROLYTIC CAPACITOR LIFETIME

The electrolytic capacitors' degradation mainly depends on two factors, operating voltage and the hot-spot temperature [21], [58]. Manufacturers often give lifetime models of aluminium electrolytic capacitors, and in this study, it is modelled as [35]:

$$L_\mathrm{c} = L_\mathrm{b} \cdot \left(4.3 - 3.3\frac{V_\mathrm{a}}{V_\mathrm{r}}\right) \cdot 2^{\frac{T_\mathrm{m}-T_\mathrm{c}}{10}} \quad (17)$$

where L_b is the rated capacitor lifetime, V_a is the applied voltage and V_r is rated voltage, T_m is the maximum rated core temperature, and T_c the operating core temperature [35]. T_m and L_b are related to the capacitor packaging and manufacturing, as specified by the manufacturer [35]. The operating hot-spot temperature, T_c, is estimated based on the capacitor Equivalent Series Resistance (ESR), the thermal resistance Z_th, both from data-sheet, and on the current flowing through the capacitor. In this regard, the full harmonic spectrum of the DC-link current, $I_\mathrm{cap,h}$, and the ESR_h variation according to the current harmonic frequency h have to be considered [35]:

$$T_\mathrm{c} = T_\mathrm{a} + 1.5 \cdot Z_\mathrm{th} \cdot \left(\sum_{h=1}^{\infty} I_{\mathrm{cap},h}^2 \cdot \mathrm{ESR}_h + I_\mathrm{leak}(V_\mathrm{op}) \cdot V_\mathrm{op}\right), \quad (18)$$

where I_leak is the capacitor leakage current as function of V_op, given by the datasheet and V_op the operating voltage [51]. When (18) is adopted for lifetime estimation purposes, the capacitor manufacturer recommends the introduction of the coefficient 1.5, so that the heat rise due to current ripple weights more than the ambient temperature T_a effect [35].

Given the hot-spot temperature profile, the accumulated damage can be determined through Miner's rule [59]:

$$CL_\mathrm{c} = \sum_{i=1}^{K} \frac{t_i}{L_{\mathrm{c},i}}, \quad (19)$$

where t_i is the time during which the capacitor is operating in

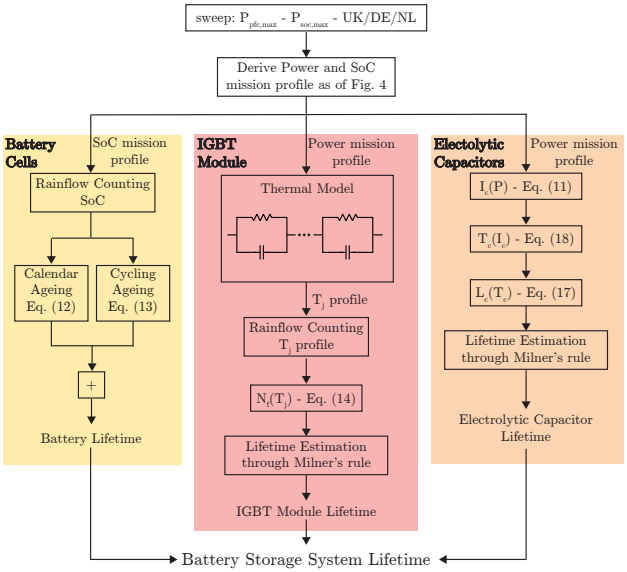

FIGURE 9. Methodology used for the lifetime estimation of electrochemical storage, semiconductor modules, and electrolytic capacitors.

a specific condition i and $L_{\mathrm{c},i}$ is the lifetime at this operating condition.

V. LIFETIME EVALUATION METHODOLOGY

The procedure adopted for evaluating the system lifetime is illustrated in Fig. 9. Starting from the droop logic and the frequency trends shown respectively in Fig. 2 and Fig. 3, the output power of the BESS is calculated. The algorithm for PFR provision is illustrated in Fig. 4. As discusses in Section II, this procedure is repeated varying the power sharing between PFR $P_{\mathrm{pfr,max}}$ and SoC management $P_{\mathrm{SoC,max}}$, respecting (1). Therefore, starting from the frequency trend, one year power and SoC mission profiles are defined, as detailed in Section II. The SoC profiles are then decomposed between idling time, when the battery system is not exchanging power with the grid, and cycling time. The idling time and SoC levels are substituted in (12) to estimate the yearly calendar degradation. A rainflow counting algorithm is applied to the cycling profile and so the equivalent cycles performed by the battery during the year are found [60]. These are substituted in (13) to determine the battery's capacity fading due to power cycling. The yearly capacity fading is derived adding the contribution of calendar and cycling ageing. Finally, the storage lifetime is obtained estimating when the capacity fading reaches 20% and thus, its EoL.

The output power found through the algorithm shown in Fig. 4 is the main input for the lifetime estimation of the IGBT modules junction temperature and of the electrolytic capacitors. At the first iteration the IGBT module junction temperature is considered 40 °C, the reference temperature of the air cooling system. For each following iteration, given the semiconductors junction temperatures and the converter output power, the IGBT and diode losses can be estimated through the loss-maps generated with (2)-(5), of which an

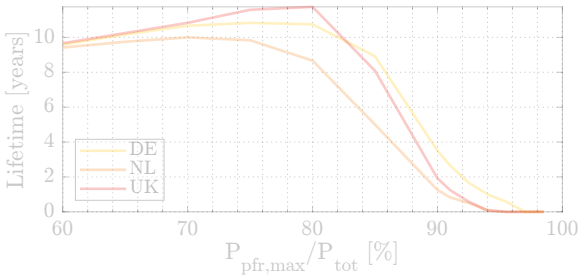

FIGURE 10. Battery cells' lifetime varying the percentage of the total power used for PFR provision, $P_{\mathrm{pfr,max}}$ in the case scenarios of Germany, the Netherlands and the UK.

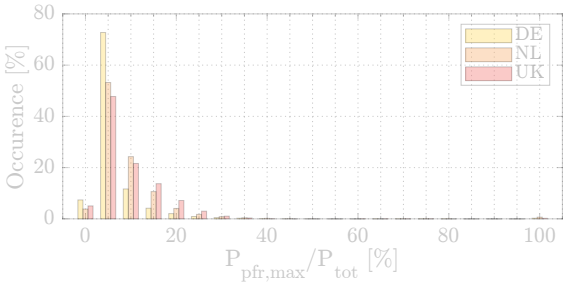

FIGURE 11. Time distribution of the BESS output power for PFR provision operating with $P_{\mathrm{pfr,max}}$=150 kW in the case scenarios of Germany, the Netherlands and the UK.

example is shown in Fig. 7. Once derived the semiconductor power losses, the temperature of heatsink, power module case, and chip die junctions can be updated through the Foster thermal model.

Once the last iteration is reached and the thermal profile of the semiconductors junction is derived, this can be decomposed in equivalent thermal cycles through a rainflow counting algorithm [60]. Number of cycles to failure, $N_{f,p}$, for the specific cycles are calculated through (14). Then, the consumed lifetime of the power module $CL_{\mathrm{s,year}}$ is estimated summing the contribution of each cycle p, $CL_{\mathrm{s,year}} = \sum_{i=1}^{N} CL_{\mathrm{s},i}$, and its lifetime through the reciprocal of the yearly consumed lifetime:

$$L_{\mathrm{s}} = \frac{1}{\sum_{p=1}^{N} CL_{\mathrm{s},p}}. \tag{20}$$

Regarding the electrolytic capacitor lifetime estimation, the capacitors current I_{dcl} can be estimated through (11) and starting from the output power and SoC mission profile. Then, the current flowing in each capacitor is found dividing I_{dcl} with the number of parallel capacitors strings. The current profile through the capacitors gives the hot-spot temperature profile that, implemented in (19), gives the capacitor wear due to the operation. Following a similar procedure to the one of the IGBT modules, the capacitor lifetime is calculated as the reciprocal of its consumed lifetime CL_{c}, as described in Section IV.

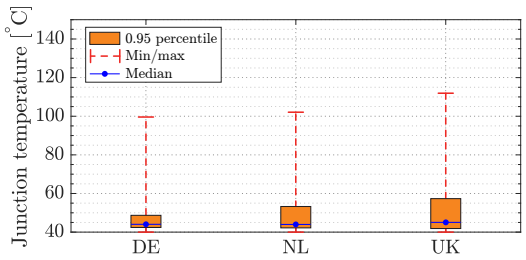

FIGURE 12. Estimated junction temperature analysis of the BESS's IGBTs providing PFR in the case scenarios of Germany, the Netherlands and the UK.

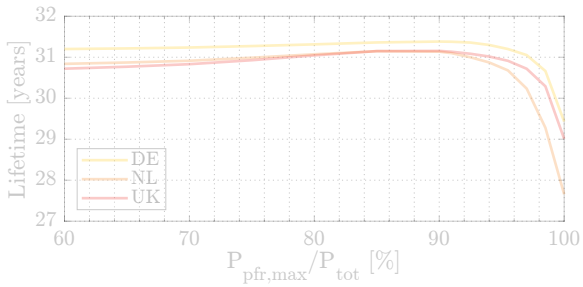

FIGURE 13. Electrolytic capacitor lifetime varying the percentage of the total power used for the provision of frequency regulation in the case scenarios of Germany, the Netherlands and the UK.

A. RESULTS AND DISCUSSION

The BESS mission profile is generated varying fraction of power assigned to PFR $P_{\mathrm{pfr,max}}$ and the one assigned to the SoC management $P_{\mathrm{SoC,max}}$ following the algorithm described in Section II.

Running the procedure detailed in Section V and Fig. 9, the electrochemical storage lifetime is estimated, and shown in Fig. 10. The results show that reducing the power reserved for PFR, $P_{\mathrm{pfr,max}}$, the battery bank lifetime can be extended, reaching the peak at around $P_{\mathrm{pfr,max}}$ equal to 70%-80% P_{tot}. However, by doing so, the revenues would decrease, since the payment scheme depends on the power bid in the tenders, $P_{\mathrm{pfr,max}}$, as it will be discussed in the following section. The lifetime of the IGBT modules of the VSC is dependent on the junction temperature profile. These IGBT and Diode temperature profiles are estimated following the methodology detailed in Section IV-B and in Fig. 9.

As shown in Fig. 11 analyzing the BESS power mission profile for $P_{\mathrm{pfr,max}}$=150 kW, it can be seen that around 95% of the time during the year the system operates at a very low partial load, $\leq$20% of the total rated output power, due to the nature of the P-f droop curves and the usually low frequency variations observed in the network. Therefore, the very low power utilization of this functionality inevitably leads the VSC to mostly operate at low junction temperature and to only seldom reach the thermal limits. Operating at low temperature and seeing small power output variations, the IGBT and diode junction is subject to low thermal stress, when applied for this specific application. In Fig. 12 the estimated IGBT junction temperature average value and the 0.95 percentile over the yearly load profile are shown and they can be seen to be very low. However, the derating of the cooling aggregate or of the semiconductor for reducing system costs is not a feasible option, since the BESS has to be capable to deliver the full power and as can be seen in Fig. 12 the IGBTs' junction can reach high temperature values, although sporadically.

Such low thermal stress, as expressed in (14) and so by the manufacturer [33], [34], leads to low semiconductor degradation. Therefore it is found that for BESS VSC performing PFR the IGBT modules are not strongly subject to degradation due to the normal operation. Other causes of failure, related for example to the environment conditions or grid transients, however remain [22].

The electrolytic capacitors also encounter a similar lifetime trend to the one shown by the electrochemical storage and the IGBT modules. As it is possible to see in Fig. 13, the reduction of $P_{\mathrm{pfr,max}}$ leads to an increase of the lifetime. Nonetheless, the lifetime extension is less pronounced than the one seen by the electrochemical storage.

TABLE 4. Economic analysis parameters

Parameter	Value
Inflation rate	$r = 2.5\%$
Battery cost	330 €/kWh
PEC+BoP cost	150 €/kW
O&M costs	4.5 €/kWh/year
Average FCR price (NL)$^{+}$	19.08 €/h/MW
Average PCR price (DE)$^{+}$	12.77 €/h/MW
Average DLH price (UK)$^{++}$	7.22 £/h/MW

$^{+}$ data extracted from [61], $^{++}$ data extracted from [38]

VI. ECONOMIC ANALYSIS

The market for Lithium-ion batteries is rapidly growing, due also to increased demand for electric vehicles and stationary storage applications, reporting a 75% decrease in battery pack's price from 2013 to 2019 [5], [62], [63]. For this study, the capital cost of electrochemical storage has been considered 330 €/kWh, according to the latest published report the US National Renewable Energy Laboratory [64]. The operation and maintenance (O&M) cost are set to 4.5€/kWh/year [17]. The cost for the Power Electronics Converter (PEC) and the Balance of the Plant (BoP) has been derived according to the solar utility market, since utility scale VSCs of photovoltaic generators are similar systems to the ones used in BESS, and fixed to 150€/kW [65], [66].

The remuneration scheme for the PFR provision in the selected countries foresees a payment to the service provider proportional to the regulating power and to the time of provision accepted in the tender, the price is then specified as €/MW/h. Germany fully contracts its regulating power through a common auction between several central European countries. The Netherlands participates in the common auc-

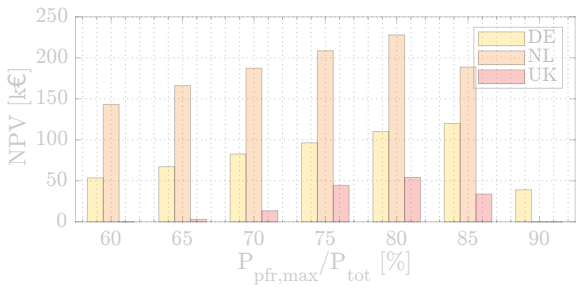

FIGURE 14. NPV over a 25 year project duration of a BESS systems rated 150kW/150kWh varying the fraction of the maximum power allocated for PFR, $P_{\mathrm{pfr,max}}$.

tion as well, however it separately contracts a fraction of its total regulating power in a national auction. According to the documentation provided by the TSOs, the average contracted price for PFR in 2018 was of 19.08 €/MW/h for the Netherlands and of 12.77 €/MW/h for the joint central European auction. In the UK a similar remuneration scheme is provided in the Phase 2 auction trial, which is an innovation project which is procuring frequency regulation products through the EPEX SPOT Auction Platform [38]. The auctions for the procuring of Dynamic Low High (DLH) frequency products, technically similar to PFR, saw an average price of 7.22 £/MW/h, which is significantly lower than the prices seen in Germany and the Netherlands.

According to the investment cost and remuneration prices here discussed and summarized in Table 4, the Net Present Value (NPV) and break-even year of a BESS providing PFR in three case scenario have been evaluated. The NPV calculation was based on a time horizon of 25 years, compatible with the electrolytic capacitors and IGBT modules lifetime, as detailed in Section IV, and on a discount rate r of 2.5% [65]:

$$\mathrm{NPV} = \sum_{t=1}^{25} \frac{R_t}{(1+r)^t} \tag{21}$$

The yearly revenue parameter, R_t, reflects the income due to PFR provision, proportional to $P_{\mathrm{pfr,max}}$, the percentage of the total power allocated for PFR, the investment and O&M costs, as detailed in Table 4, and the costs associated to the components replacements, where the replacement times are derived according to Section V.

The NPV is calculated for different $P_{\mathrm{pfr,max}}$ percentages. As already mentioned, the revenues deriving from PFR provisions are proportional to $P_{\mathrm{pfr,max}}$, thus higher $P_{\mathrm{pfr,max}}$ gives higher revenues, however, components' wear increases as well, leading to earlier replacements of the BESS's components, as illustrated in Fig. 10 and Sections V. In Fig. 14 it can be seen that the NPV presents an optimal value, so a point where the system shows the highest profitability. However, comparing these optimal points, with the results of Fig. 10 and 13 it is possible to see that the $P_{\mathrm{pfr,max}}$ value that leads to the highest NPV is not necessarily the one that leads to the lowest components degradation. It is also clear that such functionality is profitable in each country, since it is possible to find a positive NPV, however, the case of the Netherlands is the one that leads to the highest revenues, due to the higher remuneration price [61].

VII. CONCLUSION

This paper has analyzed the provision of PFR through BESSs in three case scenarios reflecting the technical and economical regulation of Germany, the UK, and the Netherlands. The lifetime of the main BESS components subject to wear, the electrochemical storage, the IGBT modules, and the electrolytic capacitors, have been investigated in the different scenarios. As it has been illustrated in Section V, the component that is subject to faster degradation is the electrochemical storage. Its lifetime peaks at 10-11 years, depending on the case scenario. The other two components whose lifetime has been investigated, electrolytic capacitors and IGBT modules, do not show significant wear due to the operation, when applied in BESS performing PFR, due to the very low power utilization of such functionality today. Nonetheless the methodology for the BESS lifetime estimation can be applied studying BESS lifetime when performing other functionalities.

Additionally, as detailed in the paper, the power sharing between the SoC management and PFR provision is a key variable for evaluating the BESS lifetime and the revenues deriving from the PFR provision. In this respect, it has been shown that the value of $P_{\mathrm{pfr,max}}$ that maximize the components lifetime does not necessarily coincide to the one that maximizes the BESS revenues.

Overall, the provision of PFR by means of BESS can be profitable in all the three countries analysed, with the present remuneration tariffs and BESS capital costs. Furthermore, the higher remuneration tariffs seen in the Netherlands in recent years lead to highest revenues between the analysed countries.

Future work will focus on BESSs lifetime estimation and economic benchmark when deployed for performing other grid connected services, such as the participation of energy markets, peak shaving and load, and services for the DSOs.

REFERENCES

[1] S. Peyghami, P. Palensky, and F. Blaabjerg, "An Overview on the Reliability of Modern Power Electronic Based Power Systems," IEEE Open J. Power Electron., vol. 1, no. December 2019, pp. 34–50, 2020.

[2] S. D'silva, M. Shadmand, S. Bayhan, and H. Abu-Rub, "Towards Grid of Microgrids: Seamless Transition between Grid-Connected and Islanded Modes of Operation," IEEE Open J. Ind. Electron. Soc., vol. 1, no. June, pp. 66–81, 2020.

[3] X. Liu, Y. Zhang, and K. Y. Lee, "Coordinated Distributed MPC for Load Frequency Control of Power System With Wind Farms," IEEE Trans. Ind. Electron., vol. 64, no. 6, pp. 5140–5150, 2017.

[4] A. F. Hoke, M. Shirazi, S. Chakraborty, S. Member, E. Muljadi, and D. Maksimovic, "Rapid Active Power Control of Photovoltaic Systems for Grid Frequency Support," IEEE J. Emerg. Sel. Top. Power Electron., vol. 5, no. 3, pp. 1154–1163, 2017.

[5] M. Stecca, L. Ramirez Elizondo, T. Batista Soeiro, P. Bauer, and P. Palensky, "A Comprehensive Review of the Integration of Battery Energy

Storage Systems into Distribution Networks," IEEE Open J. Ind. Electron. Soc., vol. 1, pp. 46–65, 2020.

[6] H. Qian, J. Zhang, J.-s. Lai, and W. Yu, "A High-Efficiency Grid-Tie Battery Energy Storage System," IEEE Trans. Power Electron., vol. 26, no. 3, pp. 886–896, 2011.

[7] J. Fang, H. Li, Y. Tang, and F. Blaabjerg, "On the Inertia of Future More-Electronics Power Systems," IEEE J. Emerg. Sel. Top. Power Electron., vol. 7, no. 4, pp. 2130–2146, 2019.

[8] P. V. Brogan, R. J. Best, D. J. Morrow, K. Mckinley, and M. L. Kubik, "Effect of BESS Response on Frequency and RoCoF During Underfrequency Transients," IEEE Trans. Power Syst., vol. 34, no. 1, pp. 575–583, 2019.

[9] S. Vazquez, S. M. Lukic, E. Galvan, L. G. Franquelo, and J. M. Carrasco, "Energy storage systems for transport and grid applications," IEEE Trans. Ind. Electron., vol. 57, no. 12, pp. 3881–3895, 2010.

[10] B. Mantar Gundogdu, S. Nejad, D. T. Gladwin, M. P. Foster, and D. A. Stone, "A battery energy management strategy for U.K. enhanced frequency response and triad avoidance," IEEE Trans. Ind. Electron., vol. 65, no. 12, pp. 9509–9517, 2018.

[11] L. Meng, J. Zafar, S. K. Khadem, A. Collinson, K. C. Murchie, F. Coffele, and G. M. Burt, "Fast Frequency Response from Energy Storage Systems - A Review of Grid Standards, Projects and Technical Issues," IEEE Trans. Smart Grid, vol. 11, no. 2, pp. 1566–1581, 2020.

[12] Y. G. Rebours, D. S. Kirkshen, M. Trotignon, and S. Rossignol, "A Survey of Frequency and Voltage Control Ancillary Services - Part I: Technical Features," IEEE Trans. Power Syst., vol. 22, no. 1, pp. 350–357, 2007.

[13] Y. G. Rebours, Kirs, M. Trotignon, and S. Rossignol, "A survey of frequency and voltage control ancillary services - Part II: Economic features," IEEE Trans. Power Syst., vol. 22, no. 1, pp. 358–366, 2007.

[14] M. Swierczynski, D. I. Stroe, A. I. Stan, and R. Teodorescu, "Primary frequency regulation with Li-ion battery energy storage system: A case study for Denmark," 2013 IEEE ECCE Asia Downunder - 5th IEEE Annu. Int. Energy Convers. Congr. Exhib. IEEE ECCE Asia 2013, pp. 487–492, 2013.

[15] D.-I. Stroe, V. Knap, M. Swierczynski, A.-I. Stroe, and R. Teodorescu, "Operation of a Grid-Connected Lithium-Ion Battery Energy Storage System for Primary Frequency Regulation: A Battery Lifetime Perspective," IEEE Trans. Ind. Appl., vol. 53, no. 1, pp. 430–438, jan 2017. [Online]. Available: http://ieeexplore.ieee.org/document/7588052/

[16] M. Bragard, N. Soltau, S. Thomas, R. W. D. Doncker, S. Member, N. Soltau, S. Member, S. Thomas, S. Member, and R. W. D. Doncker, "The Balance of Renewable Sources and User Demands in Grids : Power Electronics for Modular Battery Energy Storage Systems," IEEE Trans. Power Electron., vol. 25, no. 12, pp. 3049–3056, 2010.

[17] B. Lian, A. Sims, D. Yu, C. Wang, and R. W. Dunn, "Optimizing LiFePO4 Battery Energy Storage Systems for Frequency Response in the UK System," IEEE Trans. Sustain. Energy, vol. 8, no. 1, pp. 385–394, 2017.

[18] J. I. Y. Ota, T. Sato, and H. Akagi, "Enhancement of performance, availability, and flexibility of a battery energy storage system based on a modular multilevel cascaded converter (MMCC-SSBC)," IEEE Trans. Power Electron., vol. 31, no. 4, pp. 2791–2799, 2016.

[19] E. Chatzinikolaou, D. J. Rogers, S. Member, and D. J. Rogers, "A Comparison of Grid-Connected Battery Energy Storage System Designs," IEEE Trans. Power Electron., vol. 32, no. 9, pp. 6913–6923, 2017.

[20] IEEE Standards Association, "IEEE Std. 519-2014. IEEE Recommended Practice and Requirements for Harmonic Control in Electric Power Systems," pp. 1–29, 2014.

[21] H. H. Wang, P. Davari, H. H. Wang, D. Kumar, F. Zare, and F. Blaabjerg, "Lifetime Estimation of DC-Link Capacitors in Adjustable Speed Drives under Grid Voltage Unbalances," IEEE Trans. Power Electron., vol. 34, no. 5, pp. 4064–4078, 2019.

[22] S. Yang, A. Bryant, P. Mawby, S. Member, D. Xiang, L. Ran, S. Member, P. Tavner, and S. Member, "An industry-based survey of reliability in power electronic converters," IEEE Trans. Ind. Appl., vol. 47, no. 3, pp. 1441–1451, 2011.

[23] H. Huang and P. A. Mawby, "A Lifetime Estimation Technique for Voltage Source Inverters," IEEE Trans. Power Electron., vol. 28, no. 8, pp. 4113–4119, 2013.

[24] S. Peyghami, F. Blaabjerg, and P. Palensky, "Incorporating Power Electronic Converters Reliability into Modern Power System Reliability Analysis," IEEE J. Emerg. Sel. Top. Power Electron., 2020.

[25] C. Brivio, "Battery energy storage systems: Modelling, applications and design criteria," Ph.D. dissertation, 2012. [Online]. Available: http://hdl.handle.net/10589/136844

[26] E. Chemali, M. Preindl, P. Malysz, and A. Emadi, "Electrochemical and Electrostatic Energy Storage and Management Systems for Electric Drive Vehicles: State-of-the-Art Review and Future Trends," IEEE J. Emerg. Sel. Top. Power Electron., vol. 4, no. 3, pp. 1117–1134, 2016.

[27] U. Shipurkar, E. Lyrakis, K. Ma, H. Polinder, and J. A. Ferreira, "Lifetime Comparison of Power Semiconductors in Three-Level Converters for 10-MW Wind Turbine Systems," IEEE J. Emerg. Sel. Top. Power Electron., vol. 6, no. 3, pp. 1366–1377, 2018.

[28] S. Peyghami, H. Wang, P. Davari, and F. Blaabjerg, "Mission-Profile-Based System-Level Reliability Analysis in DC Microgrids," IEEE Trans. Ind. Appl., vol. 55, no. 5, pp. 5055–5067, 2019.

[29] U. Shipurkar, K. Ma, H. Polinder, F. Blaabjerg, and J. A. Ferreira, "A review of failure mechanisms in wind turbine generator systems," 2015 17th Eur. Conf. Power Electron. Appl. EPE-ECCE Eur. 2015, 2015.

[30] M. Liserre, F. Blaabjerg, T. Kerekes, K. Ma, M. Liserre, F. Blaabjerg, and T. Kerekes, "Thermal loading and lifetime estimation for power device considering mission profiles in wind power converter," IEEE Trans. Power Electron., vol. 30, no. 2, pp. 590–602, 2015.

[31] P. D. Reigosa, H. Wang, Y. Yang, and F. Blaabjerg, "Prediction of Bond Wire Fatigue of IGBTs in a PV Inverter under a Long-Term Operation," IEEE Trans. Power Electron., vol. 31, no. 10, pp. 7171–7182, 2016.

[32] J. Harikumaran, G. Migliazza, G. Buticchi, V. Madonna, P. Giangrande, A. Costabeber, P. Wheeler, and M. Galea, "Failure modes and reliability oriented system design for aerospace power electronic converters," IEEE Open J. Ind. Electron. Soc., vol. XX, pp. 1–1, 2020.

[33] R. Bayerer, T. Herrmann, T. Licht, J. Lutz, and M. Feller, "Model for Power Cycling lifetime of IGBT Modules," Integr. Power Syst. (CIPS), 2008 5th Int. Conf., pp. 1–6, 2008.

[34] A. Wintrich, N. Ulrich, T. Werner, and T. Reimann, Application Manual Power Semiconductors - SEMIKRON, 2015.

[35] Cornell Dublier, "Aluminum Electrolytic Capacitor Application Guide," Tech. Rep. [Online]. Available: http://www.cde.com/resources/catalogs/AEappGUIDE.pdf

[36] D. I. Stroe, M. Swierczynski, A. I. Stan, R. Teodorescu, and S. J. Andreasen, "Accelerated lifetime testing methodology for lifetime estimation of lithium-ion batteries used in augmented wind power plants," IEEE Trans. Ind. Appl., vol. 50, no. 6, pp. 4006–4017, 2014.

[37] D. I. Stroe, "Lifetime Models for Lithium-ion Batteries used in Virtual Power Plant Applications," Ph.D. dissertation, Aalborg University, 2014.

[38] NationalGridESO, Access on: Feb. 25 2020. [Online]. Available: https://www.nationalgrideso.com/balancing-services/frequency-response-services/historic-frequency-data

[39] Regelleistung, Access on: Feb. 25 2020. [Online]. Available: https://www.regelleistung.net/

[40] TenneT, "FCR Manual for BSPs - Requirements and procedures for supply of FCR," 2019.

[41] Netzfrequenzmessung, Access on: Feb. 25 2020. [Online]. Available: https://www.netzfrequenzmessung.de

[42] National Grid ESO, "Demand Side Flexibility Annual Report 2018," 2019. [Online]. Available: www.powerresponsive.com.

[43] National Grid, "State of Charge Management Guidance for FFR Providers," Tech. Rep., 2018. [Online]. Available: https://www.nationalgrideso.com/balancing-services/frequency-response-services/firm-frequency-response-ffr

[44] Samsung SDI, "ESS Batteries by Samsung SDI," 2019. [Online]. Available: https://www.samsungsdi.com/ess/index.html

[45] LG Chem ESS, "LG-Chem Energy Storage Li-ion NMC Battery Data Sheet," 2018.

[46] Infineon, "Infineon IGBT Modules." [Online]. Available: https://www.infineon.com/cms/en/product/power/igbt/igbt-modules/

[47] M. Stecca, T. B. Soeiro, L. R. Elizondo, P. Bauer, and P. Palensky, "Comparison of Two and Three-Level DC-AC Converters for a 100 kW Battery Energy Storage System," IEEE Int. Symp. Ind. Electron., vol. 2020-June, pp. 677–682, 2020.

[48] X. Pei, W. Zhou, and Y. Kang, "Analysis and Calculation of DC-Link Current and Voltage Ripples for Three-Phase Inverter With Unbalanced Load," IEEE Trans. Power Electron., vol. 30, no. 10, pp. 5401–5412, 2015.

[49] L. Malesani, L. Rossetto, P. Tenti, and P. Tomasin, "AC/DC/AC PWM Cnverter with Minimum Energy Storage in the DC Link," in IEEE Appl. Power Electron. Conf. Expo. - APEC, 1993, pp. 306–311.

[50] J. W. Kolar and S. D. Round, "Analytical calculation of the RMS current stress on the DC-link capacitor of voltage-PWM converter systems," IEE Proceedings-Electric Power Appl., pp. 1271–1282, 2005.

[51] Cornell Dubilier, “500C Capacitors.” [Online]. Available: https://www.cde.com/capacitors/aluminum-electrolytic/screw-terminal
[52] “Mouser electronics.” [Online]. Available: https://eu.mouser.com/
[53] J. Vetter, P. Nov, M. R. Wagner, C. Veit, P. Novák, M. R. Wagner, C. Veit, K. C. Möller, J. O. Besenhard, M. Winter, M. Wohlfahrt-Mehrens, C. Vogler, and A. Hammouche, “Ageing mechanisms in lithium-ion batteries,” J. Power Sources, vol. 147, no. 1-2, pp. 269–281, 2005.
[54] S. N. Motapon, E. Lachance, L.-A. Dessaint, and K. Al-Haddad, “A Generic Cycle Life Model for Lithium-Ion Batteries Based on Fatigue Theory and Equivalent Cycle Counting,” IEEE Open J. Ind. Electron. Soc., vol. 1, no. August, pp. 207–217, 2020.
[55] D. I. Stroe, M. Swierczynski, A. I. Stroe, R. Teodorescu, R. Laerke, and P. C. Kjaer, “Degradation behaviour of Lithium-ion batteries based on field measured frequency regulation mission profile,” 2015 IEEE Energy Convers. Congr. Expo. ECCE 2015, pp. 14–21, 2015.
[56] Infineon, “Infineon IGBT Stack.” [Online]. Available: https://www.infineon.com/cms/en/product/power/igbt/igbt-stacks-igbt-assemblies/
[57] ——, “AN2019-05 - PC and TC Diagrams,” Tech. Rep.
[58] H. Wang and F. Blaabjerg, “Reliability of capacitors for DC-link applications in power electronic converters - An overview,” IEEE Trans. Ind. Appl., vol. 50, no. 5, pp. 3569–3578, 2014.
[59] E. W. C. Wilkins, “Cumulative damage in fatigue,” in Colloq. Fatigue / Colloq. Fatigue / Kolloquium über Ermüdungsfestigkeit, W. Weibull and F. K. G. Odqvist, Eds. Berlin, Heidelberg: Springer Berlin Heidelberg, 1956, pp. 321–332.
[60] ASTM International, “ASTM E1049-85(2017) - Standard Practices for Cycle Counting in Fatigue Analysis.” 2011. [Online]. Available: https://www.astm.org/cgi-bin/resolver.cgi?E1049
[61] Tennet, “Annual Market Update 2018,” Electr. Mark. insights, 2013.
[62] BloombergNEF. [Online]. Available: https://about.bnef.com/blog/behind-scenes-take-lithium-ion-battery-prices/
[63] ——. [Online]. Available: https://about.bnef.com/blog/battery-pack-prices-fall-as-market-ramps-up-with-market-average-at-\156-kwh-in-2019/
[64] W. Cole and A. W. Frazier, “Cost Projections for Utility- Scale Battery Storage,” Golded, CO: National Renewable Energy Laboratory, Tech. Rep., 2019. [Online]. Available: https://www.nrel.gov/docs/fy19osti/73222.pdf
[65] R. Fu, D. Feldman, and R. Margolis, “U.S. Solar Photovoltaic System Cost Benchmark: Q1 2018,” National Renewable Energy Laboratory, Tech. Rep. October, 2018. [Online]. Available: https://www.nrel.gov/docs/fy16osti/66532.pdf
[66] D. Feldman, E. O’Shaughnessy, and R. Margolis, “Solar Industry Update,” National Renewable Energy Laboratory, Tech. Rep. February, 2020.